

Article

# Two-Stage Strategy for CO Removal from H<sub>2</sub>-Rich Streams over (Nano-) CuO/CeO<sub>2</sub> Structured Catalyst at Low Temperature

**Gianluca Landi** <sup>1</sup> , **Almerinda Di Benedetto** <sup>2,\*</sup> and **Luciana Lisi** <sup>1</sup><sup>1</sup> Institute of Researches on Combustion-CNR, Piazzale Tecchio 80, 80125 Naples, Italy; landi@irc.cnr.it (G.L.); lisi@irc.cnr.it (L.L.)<sup>2</sup> Dipartimento di Ingegneria Chimica, dei Materiali e della Produzione Industriale, University of Naples Federico II, Piazzale Tecchio 80, 80125 Naples, Italy

\* Correspondence: almerinda.dibenedetto@unina.it; Tel.: +39-0817682265; Fax: +39-081-5936-936

Received: 13 April 2018; Accepted: 9 May 2018; Published: 15 May 2018



**Abstract:** Proton exchange membrane (PEM) fuel cells represent one of the most interesting systems for converting hydrogen from fossil or renewable fuels into electric power at low temperature. To prevent poisoning of fuel cell anodes, CO concentration has to be reduced to 10–100 ppm. To this aim, the preliminary catalytic preferential oxidation of CO may be used, provided that the catalyst effectively oxidizes CO, limiting as much as possible the oxidation of H<sub>2</sub>. Presently, both high selectivity and CO conversion cannot be simultaneously achieved. In this work, a novel strategy for CO removal from H<sub>2</sub>-rich streams based on a CuO/CeO<sub>2</sub> reactive trap is proposed, exploiting both catalytic and adsorption properties of this material. The process occurs in two stages. In the first stage, one reactor, fed with a CO-containing stream, works as a CO-reactive adsorber, providing a CO-free mixture. In the second stage, the adsorbed CO is converted to CO<sub>2</sub> by O<sub>2</sub>. By this approach it is possible to simultaneously get CO lower than the limiting value and avoid any H<sub>2</sub> oxidation with no O<sub>2</sub> in the feed stream to PEM. Experimental tests allowed the evaluation of the kinetic parameters of all the reaction mechanism steps. Model simulations were performed at varying operating parameters, showing that the positive effect of high contact times and low CO inlet concentration is significantly affected by the non-linear behavior of the CO reactive adsorption.

**Keywords:** CO preferential oxidation; hydrogen; purification; CO trap; CuO/CeO<sub>2</sub>

## 1. Introduction

Proton exchange membrane (PEM) fuel cells represent a promising technology for electric power generation at low temperature from H<sub>2</sub>. Especially in mobile applications, the hydrogen source is, generally, an organic compound (fossil or renewable), which is converted to hydrogen in a fuel processor (FP), consisting of a reformer and one or two water gas shift reactors [1–8]. The so obtained H<sub>2</sub>-rich stream contains 0.5–1 vol.% CO, which is a poison for the fuel cell anode catalyst (Pt). To prevent catalyst deactivation, CO concentration has to be reduced to 10–100 ppm and then the stream has to be purified. To this aim, the catalytic PReferential OXidation of CO (CO-PROX) has been proposed [9–12].

CO-PROX catalysts have been studied to work under steady-state conditions and have been designed and selected to ensure high CO oxidation activity, selectivity, and stability. Pt- and Au-based catalysts have been first studied and some formulations have been proposed for commercial applications. Copper/ceria catalysts have been proposed as an alternative due to their good activity and selectivity at low temperatures [11,13–32].

The main drawback of CO-PROX is the competitive H<sub>2</sub> oxidation, showing a higher activation energy with respect to that of CO. At the high temperatures needed to obtain high CO conversions at reasonable contact times, H<sub>2</sub> oxidation becomes faster than CO oxidation [33–35]. In order to limit H<sub>2</sub> consumption, stringent control of the temperature profile is required and obtained by 2–4 adiabatic stages with intercooling [2,3,36,37] or exchanging reactors [38]. For this reason, the volume of the CO-PROX section is very large and can correspond to more than 40% [36] or 50% [39] total volume of the fuel processor.

Several efforts have been made in order to extend the temperature window corresponding to both high conversion and selectivity by doping CuO/CeO<sub>2</sub> with a proper cation [16,21,35,40–43] or developing suitable preparation methods [14,24,25,44] with successful results.

In order to ensure a wide temperature window, the required O<sub>2</sub>/CO ratio should be higher than the stoichiometric value, whatever the catalyst. At these conditions, the CO-PROX reaction outlet stream would contain excess O<sub>2</sub>, which would react with hydrogen at the PEM Pt anode. Accordingly, O<sub>2</sub> concentration should be kept lower than 10–100 ppm [45], thus increasing the sacrificial hydrogen.

In this work, we propose a novel process for CO abatement over a CuO/CeO<sub>2</sub> catalyst based on 2 steps: CO adsorption and subsequent oxidation. In the CO adsorption step, the reactor acts as a trap for CO and a CO-free H<sub>2</sub> flow exits the reactor; in the second step the reactor works as a catalytic converter with oxidation of the CO adsorbed over the catalyst. Through this process, it is possible to achieve a CO concentration lower than 100 ppm without O<sub>2</sub> at the PEM fuel cell inlet, preventing H<sub>2</sub> consumption.

This idea is based on previous papers showing that nano-ceria-based materials (CuO/CeO<sub>2</sub>) can adsorb CO at room temperature [46,47]. More recently, we showed that nanometric copper/ceria is able not only to adsorb CO but also to partially oxidize it, releasing CO<sub>2</sub> at room temperature, due to easier oxygen mobility occurring in nanometric catalyst particles and also to the promotion of CO<sub>2</sub> desorption [48].

We report both experimental tests and simulations of the proposed trap. Experiments were carried out on a structured monolith washcoated with nanometric CuO/CeO<sub>2</sub> [48].

A mechanism was proposed and the kinetic model of both the adsorption and the oxidation phases was derived. Simulations of both adsorption and oxidation reactors were carried out at varying residence times, the CO inlet concentration and the duration of the oxidation step.

#### Description of the Process

The block flow diagram (BFD) of the process here proposed is shown in Figure 1. It consists of two parallel catalytic reactors which alternatively operate as trap for CO and as reactor for the oxidation of CO adsorbed. In Figure 1, during Stage 1 Reactor 1 operates as a CO adsorber with the inlet stream coming from the FP, thus providing a CO-free exiting flow for the fuel cell, while Reactor 2 is regenerated by flowing air. During the Stage 2, the roles of the reactors are inverted.

Thus, the operating phases of each reactor are listed in the following:

- CO adsorption: During this phase, CO is adsorbed over the catalyst surface at very low temperature ( $T_1 < 100^\circ\text{C}$ ) at which H<sub>2</sub> does not interact with the catalytic sites;
- CO oxidation: CO trapped over the catalyst surface is oxidized and the CO<sub>2</sub> formed is desorbed.

From our previous study [48], we found that CO adsorption can be carried out at a temperature sufficiently lower than that activating H<sub>2</sub> oxidation ( $55\text{--}85^\circ\text{C}$ ), flowing the CO-containing mixture up to a time ensuring an exit CO concentration lower than 100 ppm. We also showed that the presence of H<sub>2</sub> has a null or even positive effect on CO adsorption/CO<sub>2</sub> formation, depending on the temperature, generating new hydroxyl groups at  $T > 80^\circ\text{C}$ , which enhances CO oxidation and adsorption over the catalyst surface.

When slightly increasing the temperature and flowing the O<sub>2</sub>/N<sub>2</sub> mixture, CO<sub>2</sub>, formed at the expense of lattice oxygen, starts desorbing and gaseous oxygen can restore the catalyst initial oxidation state.

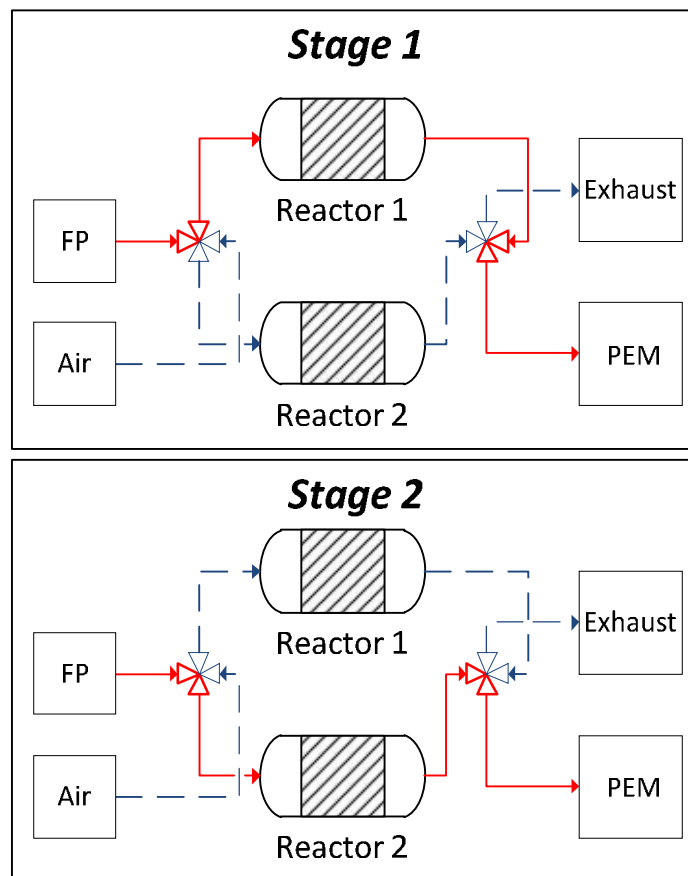


**Figure 1.** Block flow diagram (BFD) of the process. FP: Fuel Processor; PEM: proton exchange membrane. Red solid lines represent gases flowing from the FP going to reactor containing fresh/regenerated catalyst; blue dashed lines represent air flowing to reactor containing catalysts after CO adsorption.

## 2. Materials and Methods

### 2.1. Catalyst Preparation

The preparation technique of the CuO/CeO<sub>2</sub>-based monolith has been described in [49]. Briefly, a commercial honeycomb monolith (cordierite, 400 cpsi; Corning, NY 14831, USA), cut in the desired shape and dimension (cylinder; D = 16 mm; L = 12 mm), was washcoated with colloidal ceria (specific surface area (SSA) = 120 m<sup>2</sup>/g, Nyacol Nano Technologies Inc., Ashland, MA 01721, USA, CeO<sub>2</sub> particle size <20 nm) by a modified dip-coating procedure and then dried at 120 °C for 1 h and calcined in air at 450 °C for 2 h. Cycles of dip-coating followed by drying and calcination were repeated until the target ceria weight (corresponding to about 15 µm layer) was reached. A slurry containing 100% colloidal ceria was chosen to washcoat the ceramic substrate on the basis of the results reported in [49], in order to reproduce a structured catalyst with a good mechanical resistance and a high dispersion of copper.

Copper oxide was deposited onto ceria by wet impregnation using an aqueous solution of copper acetate monohydrate (Sigma-Aldrich srl, Milan, Italy); the sample was then dried at 120 °C for 1 h and calcined in air at 450 °C for 2 h again in order to decompose acetate into copper oxide. The procedure

was repeated until the desired copper oxide load (4 wt % with respect to the active layer), determined by sample weight after each cycle, was obtained.

The final catalyst ( $\text{CuO}/\text{CeO}_2$ ) amount was about 450 mg/monolith. The ICP-MS analysis (performed with an Agilent 7500CE (California USA) Instrument) revealed that the copper content (4.0 wt %) corresponded to the target load within the experimental error ( $\leq 5\%$ ).

## 2.2. Lab Test Rig

The lab-scale set-up used for CO-PROX experiments is described elsewhere [34]. It consisted of a tubular quartz reactor where the monolith, wrapped in a ceramic wool tape, is located between two mullite foams. The catalytic reactor was pre-heated using an electric tubular furnace (Lenton, UK) provided with a PID-type controller. Under the experimental conditions used in this study, a relatively flat temperature profile was recorded through three thermocouples placed inside the central channel as described in [50].

Lab experiments consisted of the following segments:

- Segment 1—Isothermal adsorption.  $T = 55^\circ\text{C}$ ,  $\text{CO} = 5000 \text{ ppm}$  in  $\text{N}_2$  flow. When the CO concentration reaches 100 ppm the reactor is by-passed.
- Segment 2—Oxidation temperature is increased up to  $100^\circ\text{C}$ , heating rate =  $10^\circ\text{C}/\text{min}$ , 5 vol %  $\text{O}_2$  in  $\text{N}_2$  flow to the reactor.
- Segment 3—Isothermal adsorption (repeatability test).

Segment 1 was repeated after Segment 2 to test the repeatability of the cycle.

The outline of the whole experiment is reported in Figure 2. A 5%  $\text{CO}/\text{N}_2$  mixture was suitably pre-mixed with pure  $\text{N}_2$  to obtain 5000 ppm CO in Segment 1, whereas pure  $\text{O}_2$  was pre-mixed with pure  $\text{N}_2$  to feed 5%  $\text{O}_2/\text{N}_2$  in Segment 2. All gas flows were controlled by MFC and were dried by passing through a  $\text{CaCl}_2$  trap before reaching a Fisher-Rosemount NGA2000 (St. Louis, MA, USA) continuous analyzer for  $\text{CO}$ ,  $\text{CO}_2$ , and  $\text{O}_2$ . The feed mixture did not contain  $\text{H}_2$  due to the negligible effect of this component at temperature  $< 80^\circ\text{C}$  [48].

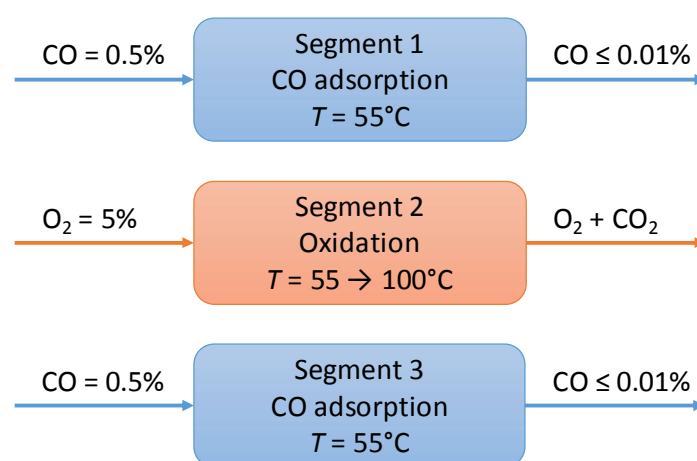


**Figure 2.** Outline of the lab experiment.

## 3. Results

In Figure 3, the temporal evolution of CO and  $\text{CO}_2$  concentrations are shown for the three segments previously described. In Table 1, the corresponding CO and  $\text{CO}_2$  amounts are given. During Segment 1, the target CO exit concentration ( $< 100 \text{ ppm}$ ) was attained for about 30 s. As observed in [48],  $\text{CO}_2$  started to be detected in the gas phase only when CO concentration rose. Consequently,  $\text{CO}_2$  concentration in the gas flow theoretically entering the fuel cell was negligible. The amount of CO

consumed during this segment was about  $4.5 \times 10^{-2}$  mmol and was mostly trapped on the catalyst surface. The corresponding CO/Cu ratio was equal to 0.19.

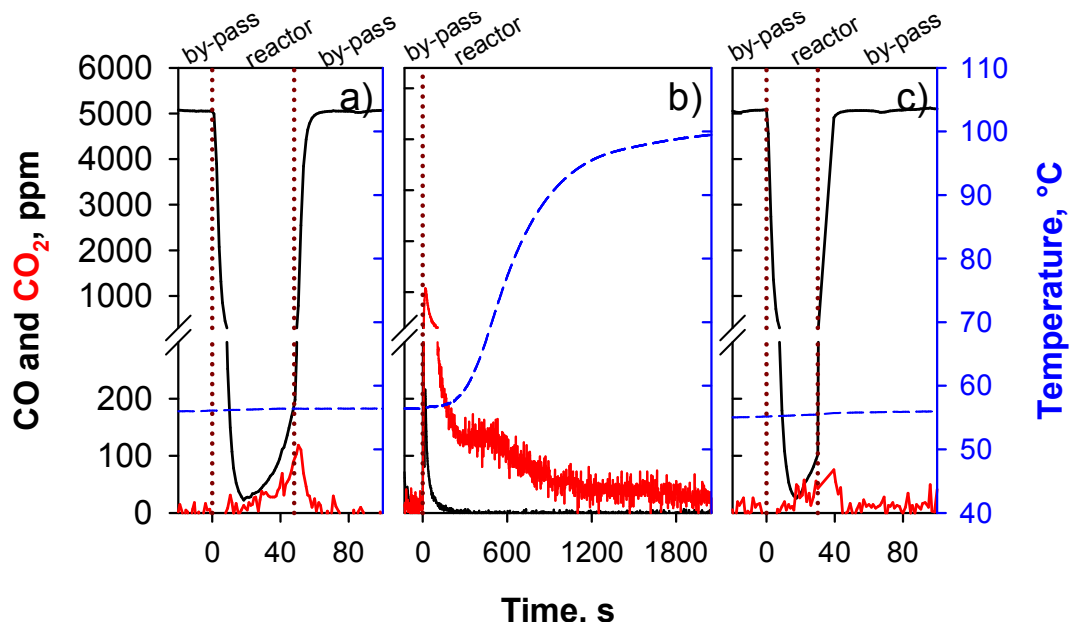


**Figure 3.** CO (black line) and CO<sub>2</sub> (red line) concentrations and temperature as function of time during segment 1 (a), 2 (b) and 3 (c).

**Table 1.** CO consumed and CO<sub>2</sub> formed in segments 1, 2 and 3.

Molecule	Segment 1	Segment 2 (Isothermal)	Segment 2 (Total)	Segment 3
	(mmol)			
CO	$4.50 \times 10^{-2}$	$0.2 \times 10^{-2}$	$0.2 \times 10^{-2}$	$2.72 \times 10^{-2}$
CO <sub>2</sub>	$0.04 \times 10^{-2}$	$1.65 \times 10^{-2}$	$3.02 \times 10^{-2}$	-

In Segment 2, a very narrow peak of CO was observed at the very beginning with a maximum value not exceeding the target exit CO concentration, whereas mainly CO<sub>2</sub> evolved. From a quantitative point of view, about  $3.0 \times 10^{-2}$  mmol of CO<sub>2</sub> were produced, corresponding to 67% of CO consumed in Segment 1, representing a very good result taking into account the low operating temperature. It is worth noting that most of the CO<sub>2</sub> evolution ( $\approx 55\%$ ) occurred in the first few minutes at 55 °C due to the positive effect of temperature on both CO oxidation (oxygen mobility) and CO<sub>2</sub> desorption rate, in agreement with our previous results [48].

When segment 1 was repeated (segment 3), a significant reduction of the time when exiting CO concentration was below the target was observed (20 s vs. 30 s). Accordingly, CO adsorbed in Segment 3 was 40% lower than that adsorbed in segment 1 and also slightly lower than the CO<sub>2</sub> evolved during segment 2. This reduction should be related to the initial state of the catalyst surface, still partially covered after the segment 2, and thus not completely available for the fresh catalyst.

Without exception, the trap provided a clean gas flow with a maximum punctual value of CO outlet concentration of 100 ppm, 100% selectivity (no H<sub>2</sub> can be oxidized under these conditions, as demonstrated in [48]) and no O<sub>2</sub> in the H<sub>2</sub>-rich stream.

## 4. Model

### 4.1. Reaction Mechanism and Kinetic Model

The results of our previous tests on CO adsorption/oxidation at room temperature provided insights into the reaction path [48].

Also based on results by others [13,14,32,43,51,52], we concluded that, most probably, CO adsorption activates the copper redox cycle between +2 and +1 oxidation states. The main role of Ce is to provide oxygen to Cu sites through easily mobile lattice oxygen.

We found that the most important parameters affecting the reaction path are the surface oxygen mobility/availability [15] and the CO<sub>2</sub> desorption rate [32]. The presence of O<sub>2</sub> activates the direct oxidation of copper and of oxygen vacancies of ceria in the area of copper sites.

According to the above findings, the following mechanism is here derived:



With the presence of O<sub>2</sub> in the gas phase, the oxidation steps of sites σ' and σ have to be considered:



In Table 2, the nature of each site in the mechanism (1)–(6) is given. In the proposed mechanism, CO is adsorbed on Cu<sup>2+</sup> sites in strict contact with ceria, causing a partial reduction of copper (and adjacent cerium atom) (step 1). CO<sub>2</sub> is then formed and transferred onto ceria sites, causing copper reduction to Cu<sup>+</sup> (and adjacent cerium reduction to Ce<sup>3+</sup>) (step 2). The CO<sub>2</sub> adsorption onto sites different from copper is in agreement with [32]. Step 3 represents CO<sub>2</sub> desorption. As reported in [48], copper re-oxidation can occur also in the absence of molecular oxygen in the gas phase at the expense of an oxygen transfer from ceria sites, leading to a surface ceria reduction (step 4). When molecular oxygen is fed, re-oxidation of the surface can occur on both copper/ceria and ceria sites (steps 5 and 6).

**Table 2.** Nature of the sites reported in the mechanism 1–6.

Symbol of Site	Nature of Site	Site Fraction Symbol
σ-O	Cu <sup>2+</sup> – O <sup>2-</sup> – Ce <sup>4+</sup>	θ <sub>1</sub>
σ-O-CO	Cu <sup>(2-δ)+</sup> – O <sup>-2</sup> – CO <sup>(δ+ε)+</sup> – Ce <sup>(4-ε)+</sup>	θ <sub>2</sub>
σ'-O-CO <sub>2</sub>	CO <sub>2</sub> – Ce <sup>4+</sup> – O <sup>2-</sup> – Ce <sup>4+</sup>	θ <sub>3</sub>
σ	Cu <sup>+</sup> – □ – Ce <sup>3+</sup>	θ <sub>4</sub>
σ'-O	Ce <sup>4+</sup> – O <sup>2-</sup> – Ce <sup>4+</sup>	θ <sub>5</sub>
σ'	Ce <sup>3+</sup> – □ – Ce <sup>3+</sup>	θ <sub>6</sub>

Based the mechanism (1)–(6), a kinetic model was developed. All steps are assumed irreversible except step 1. Rates of steps 1–6 are:

$$R_1 = k_1 \theta_1 C_{CO} \quad (7)$$

$$R_{-1} = k_{-1} \theta_2 \theta_1 \quad (8)$$

$$R_2 = k_2 \theta_2 \theta_5 \quad (9)$$

$$R_3 = k_3 \theta_3 \quad (10)$$

$$R_4 = k_4 \theta_4 \theta_5 \quad (11)$$

$$R_5 = k_5 \theta_6 C_{O2}^n \quad (12)$$

$$R_6 = k_6 \theta_4 C_{O2}^n \quad (13)$$

where  $\theta_{1-6}$  are the fractions of sites with respect to the total number of sites (Table 2).

We assumed that both the activation energy ( $E_i$ ) and the frequency factor ( $k^\circ_i$ ) are not dependent of the adsorption degree (Redhead Approximation).

Thus, the kinetic constant of step (i) is:

$$k_i = k^\circ_i \exp(-E_i/RT) \quad (14)$$

The unsteady balance equations on the fraction ( $\theta_1, \theta_2, \theta_3$  and  $\theta_5$ ) read:

$$\frac{d\theta_1}{dt} = -R_1 + R_{-1} + R_4 + R_6 \quad (15)$$

$$\frac{d\theta_2}{dt} = R_1 - R_{-1} - R_2 \quad (16)$$

$$\frac{d\theta_3}{dt} = +R_2 - R_3 \quad (17)$$

$$\frac{d\theta_5}{dt} = -R_2 + R_3 - R_5 + R_6 \quad (18)$$

The total sites conservation equations complete the system:

$$\theta_1 + \theta_2 + \theta_4 = \theta_{Cu}^\circ \quad (19)$$

$$\theta_3 + \theta_5 + \theta_6 = \theta_{Ce}^\circ \quad (20)$$

The initial conditions are:

$$t = 0; \theta_1 = \theta_1^\circ \quad (21)$$

$$t = 0; \theta_2 = \theta_2^\circ \quad (22)$$

$$t = 0; \theta_3 = \theta_3^\circ \quad (23)$$

$$t = 0; \theta_5 = \theta_5^\circ \quad (24)$$

Regarding the balance on gas phase species, we assumed the reactor was composed by two vessels (R) and (T) (Figure 4). The vessel R is the catalytic reactor, while T is representative of the tube connecting the reactor (R) and the analyzer, whose residence time represents the delay time between gas species' exit from the reactor and their detection in the analysis system.

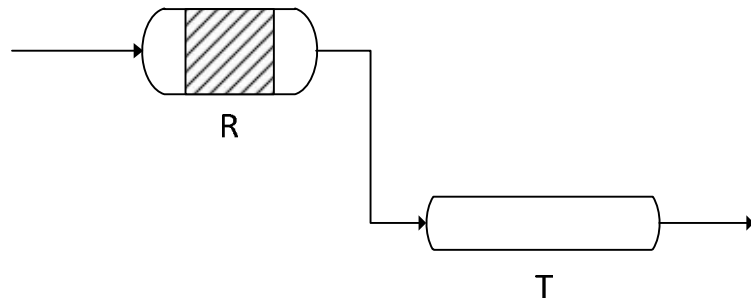


**Figure 4.** Scheme of the reactor network. R: catalytic reactor; T: reactor-analyzer connection tube.

The lab reactor used here for the tests is characterized by value of the axial Peclet (Pe) number equal to 50. This value suggests that each channel of the monolith behaves as a reactor with significant back diffusion. As a consequence, the reactor has an intermediate behavior between a plug flow reactor (PFR) and a continuous stirred tank reactor (CSTR). We used a CSTR as model reactor to simplify the fitting procedure. This choice allows a rough estimation of the kinetic parameters which can be used in the trap model to (at least qualitatively) test the idea. Further work will be focused on the development of the complete process configuration, which will take into account the real behavior of the reactor.

Furthermore, transport limitations are negligible since the kinetic regime is fully maintained by keeping the operating temperature very low (55 °C).

The CO molar balance equations in the reactor (R) and in the connecting tube (T) are the following:

**R:**

$$\frac{1}{C^\circ} \frac{dC_{CO}}{dt} - \frac{C_{CO}^{in} - C_{CO}}{C^\circ \tau_1} = -R_1 + R_{-1}, \quad (25)$$

**T:**

$$\frac{1}{C^\circ} \frac{dC_{CO}}{dt} - \frac{C_{CO}^{in} - C_{CO}}{C^\circ \tau_2} = 0. \quad (26)$$

The CO<sub>2</sub> molar balance equations are the following:

**R:**

$$\frac{1}{C^\circ} \frac{dC_{CO2}}{dt} + \frac{C_{CO2}}{C^\circ \tau_1} = R_3, \quad (27)$$

**T:**

$$\frac{1}{C^\circ} \frac{dC_{CO2}}{dt} + \frac{C_{CO2}}{C^\circ \tau_2} = 0, \quad (28)$$

where  $C^\circ$  is the total gas concentration (mol/g) and  $\tau_1$  and  $\tau_2$  are the residence times (s) of the reactor R and the connecting tube T respectively.

The O<sub>2</sub> molar balance equations are the following:

**R:**

$$\frac{1}{C^\circ} \frac{dC_{O2}}{dt} - \frac{C_{O2}^{in} - C_{O2}}{C^\circ \tau_1} = -1/2R_5 - 1/2R_6, \quad (29)$$

**T:**

$$\frac{1}{C^\circ} \frac{dC_{O2}}{dt} - \frac{C_{O2}^{in} - C_{O2}}{C^\circ \tau_1} = 0. \quad (30)$$

The initial conditions of the CO, CO<sub>2</sub>, and O<sub>2</sub> molar balances are the following:

$$t = 0; C_{CO2} = 0 \quad (31)$$

$$t = 0; C_{CO} = 0 \quad (32)$$

$$t = 0; C_{O2} = 0, \quad (33)$$

when simulating the oxidation phase, the initial conditions for both the site concentrations ( $\theta_i$ ) and the gas phase molar concentration ( $C_i$ ) are the final values corresponding to the adsorption phase simulation. The model equations with the initial conditions were solved by means of the Runge-Kutta method.

To quantify the differences between the experimental and the model curves, we computed the root mean square error (SRMSE) normalized by the maximum value of the experimental curve ( $C_{max}$ ) [53]:

$$SRMSE = \frac{1}{C_{max}} \sqrt{\frac{1}{N} \sum_{i=1}^N (C_{exp}(i) - C_{model}(i))^2} \quad (34)$$

According to Kanervo et al. [53], if SRMSE ≤ 0.045 then the experimental and modeling curves may be considered in good agreement.

#### 4.2. Model Validation

In order to derive the kinetic parameter values, we preliminary fitted the experimental curves of the adsorption phase, in the absence of O<sub>2</sub> in the feed on the basis of data reported in [48] that were obtained at different temperatures and contact times. The values of kinetic parameters obtained are given in Table 3, together with the value of the regression factor, SRMSE.

**Table 3.** Kinetic parameters of steps 1–4.

Step	Kinetic Constant ( $k_i$ , 1/s)	Activation Energy (E <sub>i</sub> , J/K mol)
1	120	30,000
-1	60,000	33,000
2	10,000	32,000
3	6000	32,000
4	50	25,000
Root mean square error (SRMSE) = 0.021		

The SRMSE value suggests that the agreement between the two curves is quite satisfactory being  $\leq 0.045$  [53].

In Figure 5a, the comparison between the experimental and the model outlet CO and CO<sub>2</sub> concentrations during the adsorption are shown as a function of time. In Figure 5b, the reaction rate of CO consumption is compared with the experimental rate. Both figures show a very good agreement between experimental and model results.

Trends of the site concentrations were also computed from the model. In Figure 5c the temporal evolution of the site concentrations is shown.

It is found that at the end of the reaction, Cu sites in the oxidized form are completely consumed ( $\theta_1 = 0$ ). Parts of them are covered by CO ( $\theta_2$ ) and parts of them are simply reduced ( $\theta_4$ ).

It is worth noting that CO<sub>2</sub> is still present over the Ce sites ( $\theta_3$ ) and the Ce sites are only partially reduced, since the concentration of oxidized sites is higher than zero ( $\theta_5$ ).

Furthermore, from the trend of  $\theta_5$ , it is possible to follow the O transfer from Ce sites to Cu sites, which allows for CO adsorption.  $\theta_5$  ( $\sigma'$ -O) first decreases, driving the CO<sub>2</sub> formation through step 2 and then it increases, since it is restored by CO<sub>2</sub> desorption (step 3).

The O transfer is then facilitated by the CO-CO<sub>2</sub> cycle occurring over the catalyst surface and by step 5, which eventually allows for the reduction of Ce based sites ( $\theta_5 \rightarrow \theta_6$ ). At the end of the run (~400 s), CO<sub>2</sub> is almost completely desorbed ( $\theta_3 \approx 0$ ). From these results, it turns out that the controlling parameter is O availability/mobility.

After the adsorption phase, O<sub>2</sub> is fed to the reactor in order to re-oxidize the catalyst sites.

According to our trap experiment (Figure 3), the adsorption step is stopped at about 45 s (CO  $\approx$  100 ppm). To quantify the kinetic parameters of the oxidation reactions of the mechanism (steps 6 and 7), we fitted the experimental curves.

It is worth noting that in the experiments there is a time delay between the adsorption phase and the oxidation phase in which the catalyst is under CO/CO<sub>2</sub>/N<sub>2</sub> atmosphere at isothermal conditions.

In Figure 6, the comparison between the experimental and the model curves during the oxidation are shown.

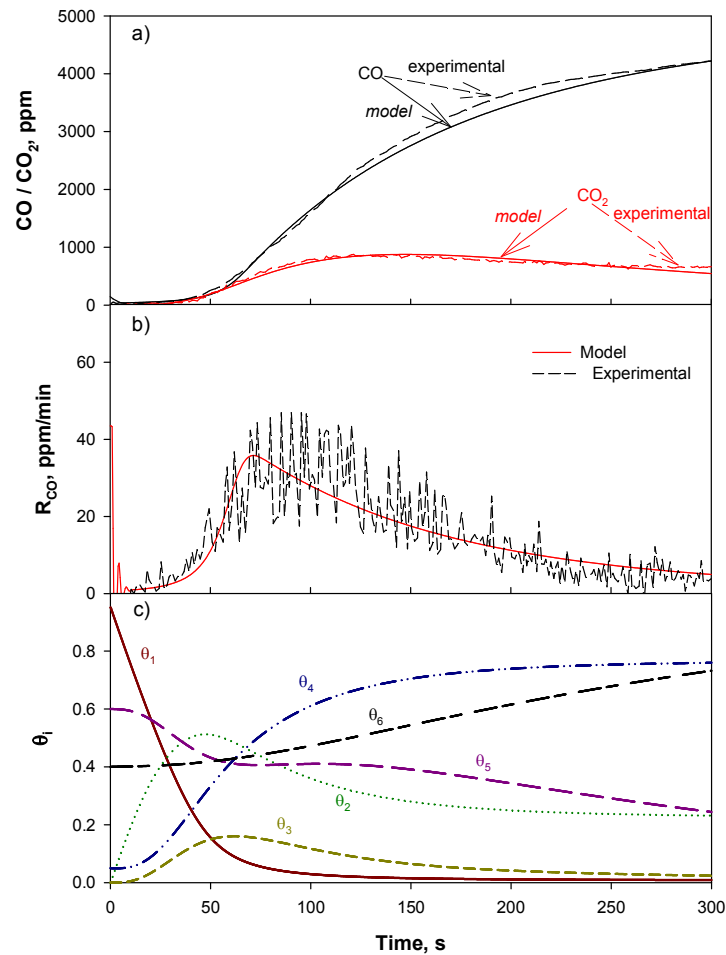


**Figure 5.** Experimental (dashed lines) and model (solid lines) CO and CO<sub>2</sub> concentrations (a) and CO reaction rate (b) as a function of time during the adsorption. Site concentrations (c) as a function of time during the adsorption.  $T = 55\text{ }^{\circ}\text{C}$ ,  $\text{CO}^{in} = 5000\text{ ppm}$  ( $\theta_i$  = fraction of site i).

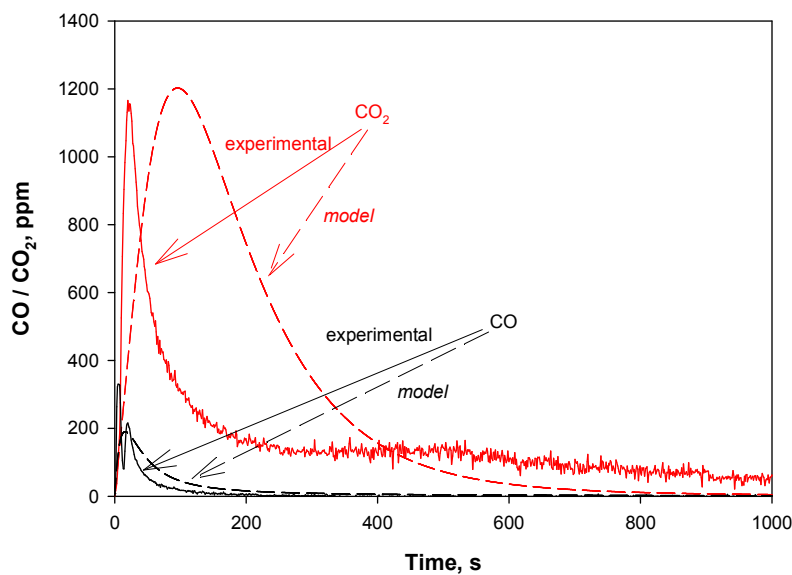


**Figure 6.** Experimental (solid lines) and model (dashed lines) CO and CO<sub>2</sub> concentrations as a function of time during the oxidation.  $T = 55\text{ }^{\circ}\text{C}$ ,  $\text{CO}^{in} = 0\text{ ppm}$ ,  $\text{O}_2^{in} = 5\text{ vol.\%}$ .

The agreement between the experimental and the model curves is poor.

This deviation could be explained on the basis of the model of the reactor we used. As previously discussed, the experimental reactor exhibits an intermediate behavior between a PFR and a CSTR, being characterized by a significant back diffusion. The presence of axial dispersion causes an increase of the deviation of the curves from a pulse, which is typical of a PFR reactor. Nevertheless, the aim of the model is not to fit the experimental data but rather to get reliable kinetic parameters to test the idea of the trap configuration.

From the comparison between the curves, we get the values of the kinetic constants of the oxidation step, which are given in Table 4.

**Table 4.** Kinetic parameters of steps 5 and 6.

Step	Kinetic Constant ( $k_i$ , $(\text{m}^3/\text{mol})^{0.5} \text{ s}$ )	Activation Energy ( $E_i$ , J/K mol)
5	50	21,000
6	5	22,000
SRMSE = 0.35		

As shown in Table 4, the value of SRMSE is quite high, confirming that the agreement between the experimental and the model curves is not satisfactory.

#### 4.3. Adsorption Phase: Effect of the Operating Parameters

In order to study the effect of the parameters on the performances of the adsorption phase, we computed the CO and  $\text{CO}_2$  outlet concentrations by varying the contact time and the CO inlet concentration.

In Figure 7, the CO and  $\text{CO}_2$  outlet concentrations are shown as a function of time as computed at different values of the residence time of the reactor, R.

As expected, when increasing the residence time, CO outlet concentration decreases at any given time and the time length at which CO outlet concentration is lower than 100 ppm increases. The  $\text{CO}_2$  outlet concentration increases even more than expected due to the non-linear behavior of residence time with respect to  $\text{CO}_2/\text{CO}$  ratio observed and explained in [48].

In Figure 8, the time at which CO outlet concentration is equal to 100 ppm is plotted versus the residence time of reactor R.

When increasing the residence time, the duration of the adsorption phase may potentially increase up to more than 1 min for a residence time of 300 s. Nevertheless, the figure also shows clear changes of the slope by increasing the residence time, due to non-linear behavior of the reactive adsorption on the  $\text{CuO}/\text{CeO}_2$  catalyst [48].

In Figure 9, the CO and  $\text{CO}_2$  outlet concentrations are plotted versus time as calculated at different values of CO inlet concentration. When increasing the CO content in the feed mixture, the time at 100 ppm significantly decreases, as expected. Nevertheless, the same does not occur for  $\text{CO}_2$  at high values of CO inlet concentration. The amount of  $\text{CO}_2$  released at 5000 ppm CO approaches that released for 7000 ppm. This effect can be considered opposite to that produced by the increase of residence time observed in [1] and highlights the limiting step of  $\text{CO}_2$  oxidation and desorption. In other words, transfer of  $\text{CO}_2$  from  $\theta_2$  to  $\theta_3$  sites with subsequent  $\text{CO}_2$  desorption and reduction of  $\theta_1$  sites into  $\theta_4$  sites has a plateau value likely related to vicinity of  $\text{Cu}^{2+}-\text{O}^{2-}-\text{Ce}^{4+}$  sites and  $\text{Ce}^{4+}-\text{O}^{2-}-\text{Ce}^{4+}$  sites, which is a measure of copper dispersion. On the other hand, CO adsorption can still continue on copper/ceria sites not able to oxidize CO and transfer  $\text{CO}_2$ .

In Figure 10, the time at which the CO outlet concentration is equal to 100 ppm is plotted versus the CO inlet concentration, showing that upon increasing the CO inlet concentration, the time duration of the adsorption phase should be lower and lower. It is worth noting that due to the non-linear

behavior of the CO reactive adsorption on the CuO/CeO<sub>2</sub> catalyst, the adsorption time is significantly higher than expected in absence of CO reaction and CO<sub>2</sub> release (dashed line in Figure 10).

In Figure 11, the site concentrations are plotted as calculated for all the CO<sup>in</sup> concentrations. It appears that at the highest values of CO<sup>in</sup> (5000 and 7000 ppm), the sites distribution almost overlaps, suggesting a saturation of the catalyst sites.

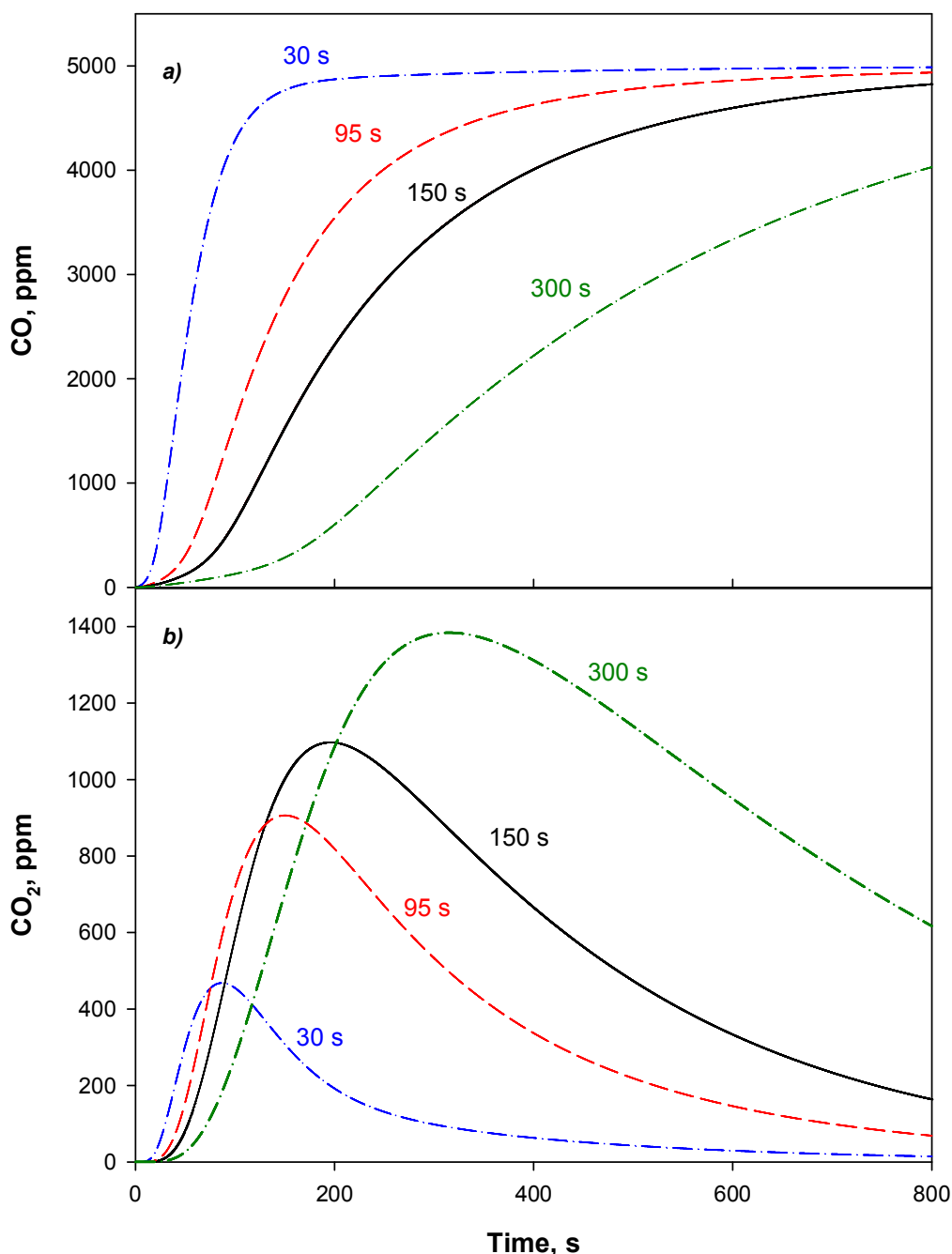


**Figure 7.** CO (a) and CO<sub>2</sub> (b) outlet concentrations versus time at different values of the residence time (model results). CO<sup>in</sup> = 5000 ppm; T = 55 °C.

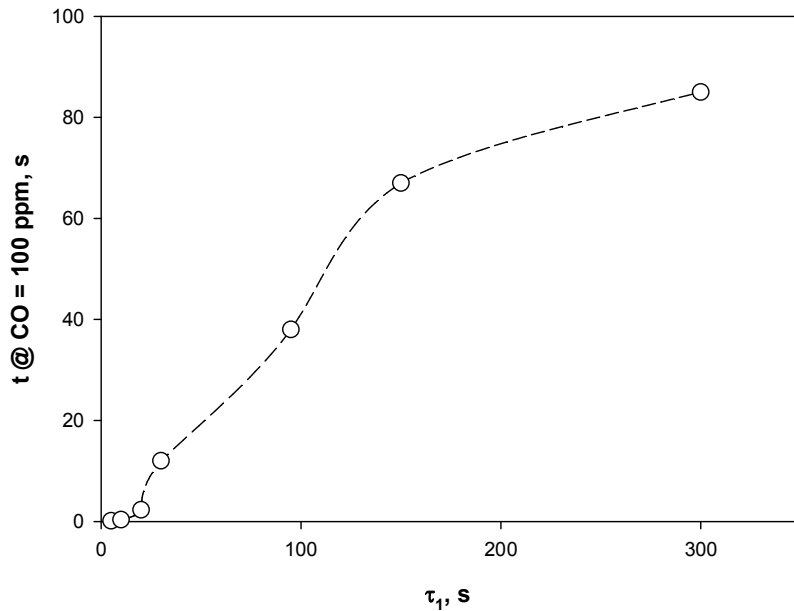


**Figure 8.** Time at which CO outlet concentration is equal to 100 ppm as a function of the reactor residence time,  $\tau_1$ .  $CO^{in} = 5000 \text{ ppm}$ ;  $T = 55^\circ\text{C}$ .

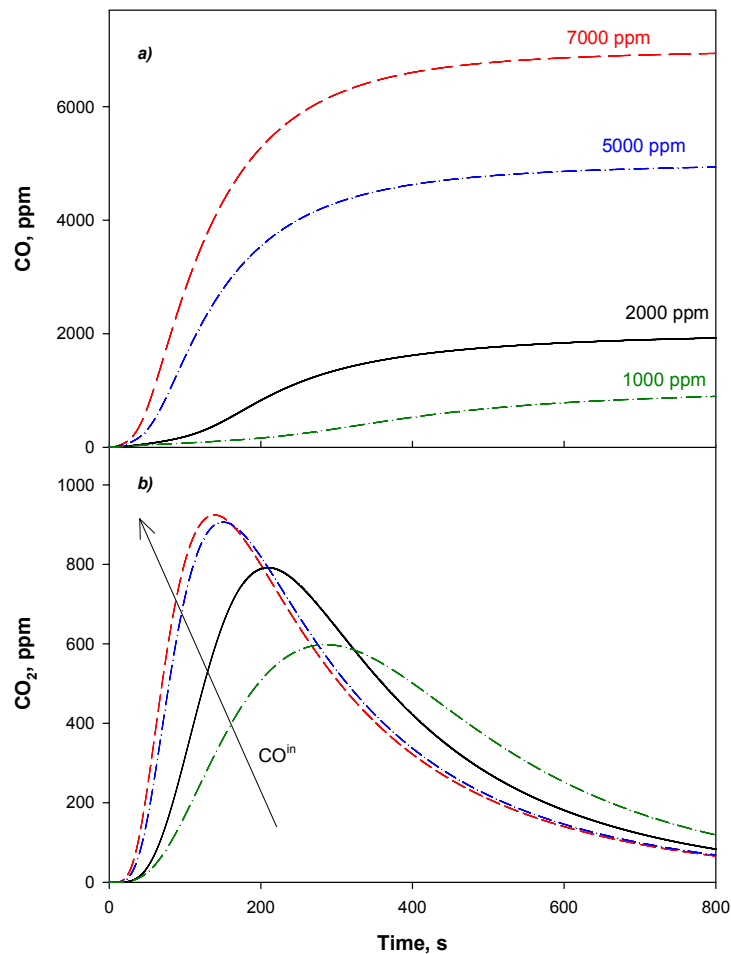


**Figure 9.** CO (a) and CO<sub>2</sub> (b) outlet concentrations versus time at different values of the CO inlet concentration (model results).  $\tau = 95 \text{ s}$ ;  $T = 55^\circ\text{C}$ .

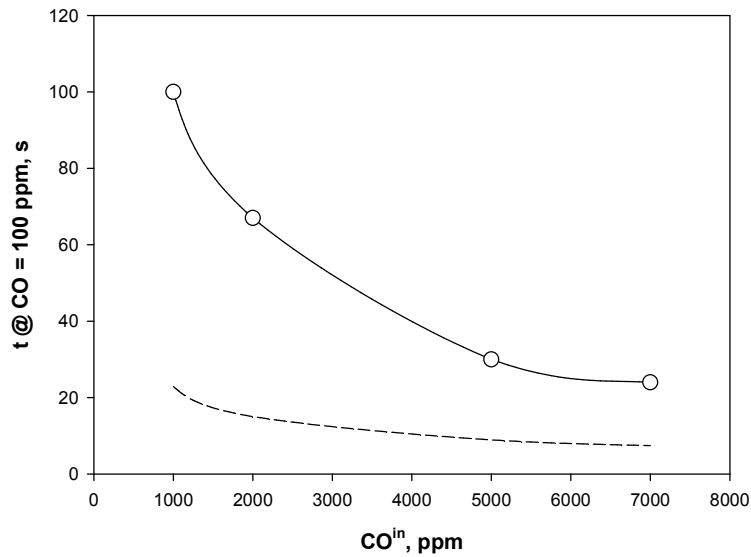


**Figure 10.** Time at which CO outlet concentration is equal to 100 ppm as function of CO inlet concentration. The dashed line represents the time at which CO outlet concentration is equal to 100 ppm in the case of non-reactive adsorption ( $R_i = 0$ ).

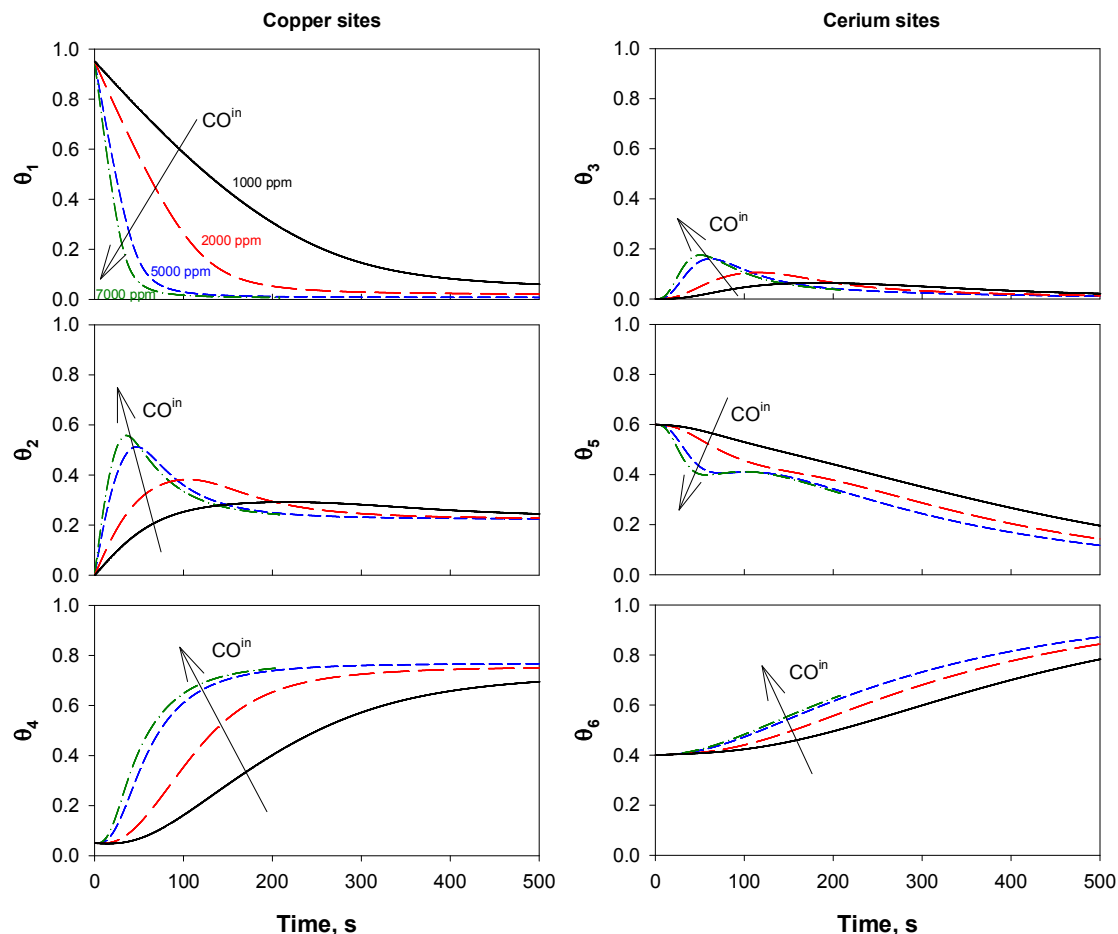


**Figure 11.** Site fraction concentrations ( $\theta_i$ ) as a function of time as computed at different values of the CO inlet concentration (reported on the curves of the top left figure). (Refer to Table 2 for the nature of sites corresponding to each  $\theta_i$ ).

In Figure 12, results of simulations of the adsorption phase, varying both residence time and CO inlet concentration, are summarized by the plane residence time/CO inlet concentration. The bubble dimension is proportional to the time at which CO outlet concentration is equal to 100 ppm.

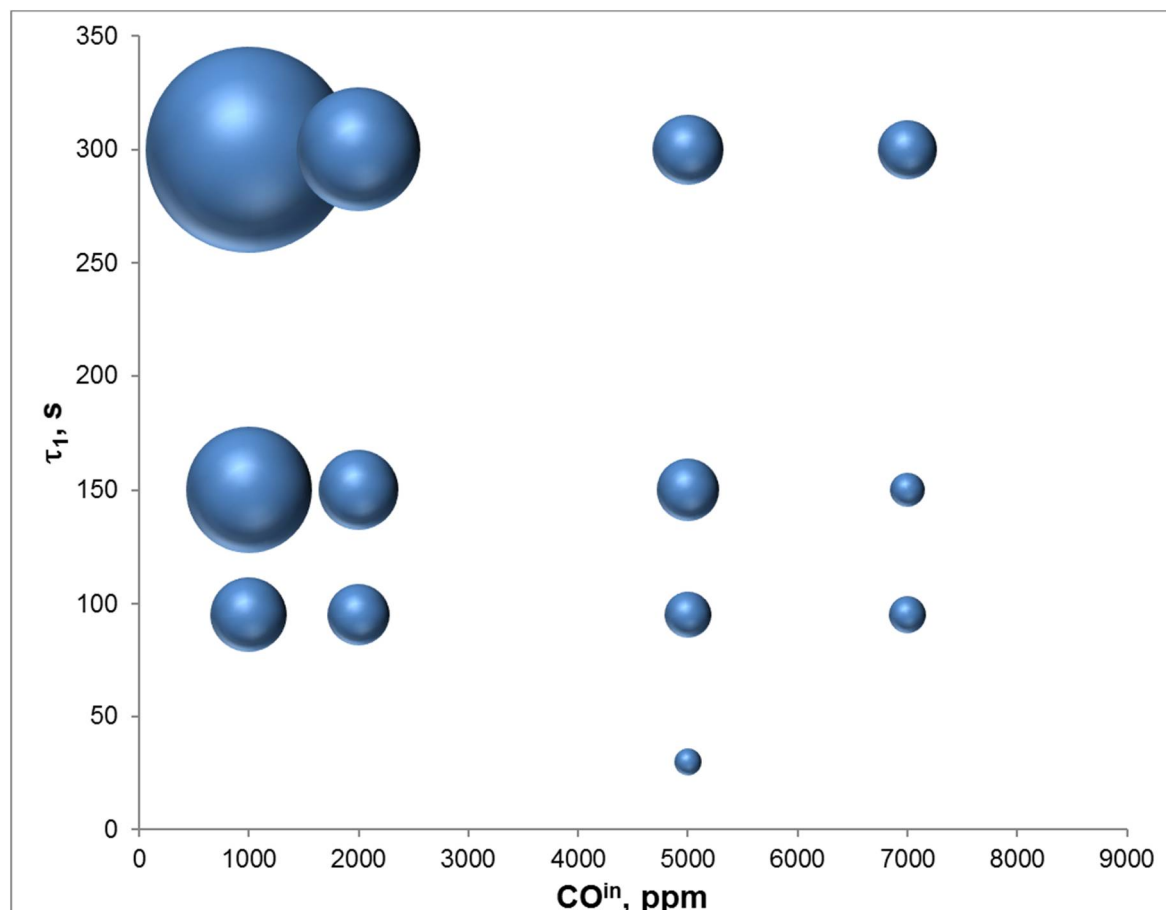


**Figure 12.** Plane residence time/CO inlet concentration, the bubble dimension is proportional to the time at which CO outlet concentration is equal to 100 ppm.

It is worth noting that the best conditions are attained at low CO inlet concentration and high residence time.

#### 4.4. Trap Simulation

The effect of the time length of the oxidation phase is fundamental for an effective regeneration of the catalyst.

To this end, we simulated the complete (isothermal) trap, by setting  $\text{CO}^{\text{in}} = 5000 \text{ ppm}$  and  $\tau_1 = 95 \text{ s}$ . In Figure 13,  $\text{CO}_2$  (a) and CO (b), are shown as a function of time as obtained by simulating both the adsorption (Phase I) and the oxidation (Phase II) step.

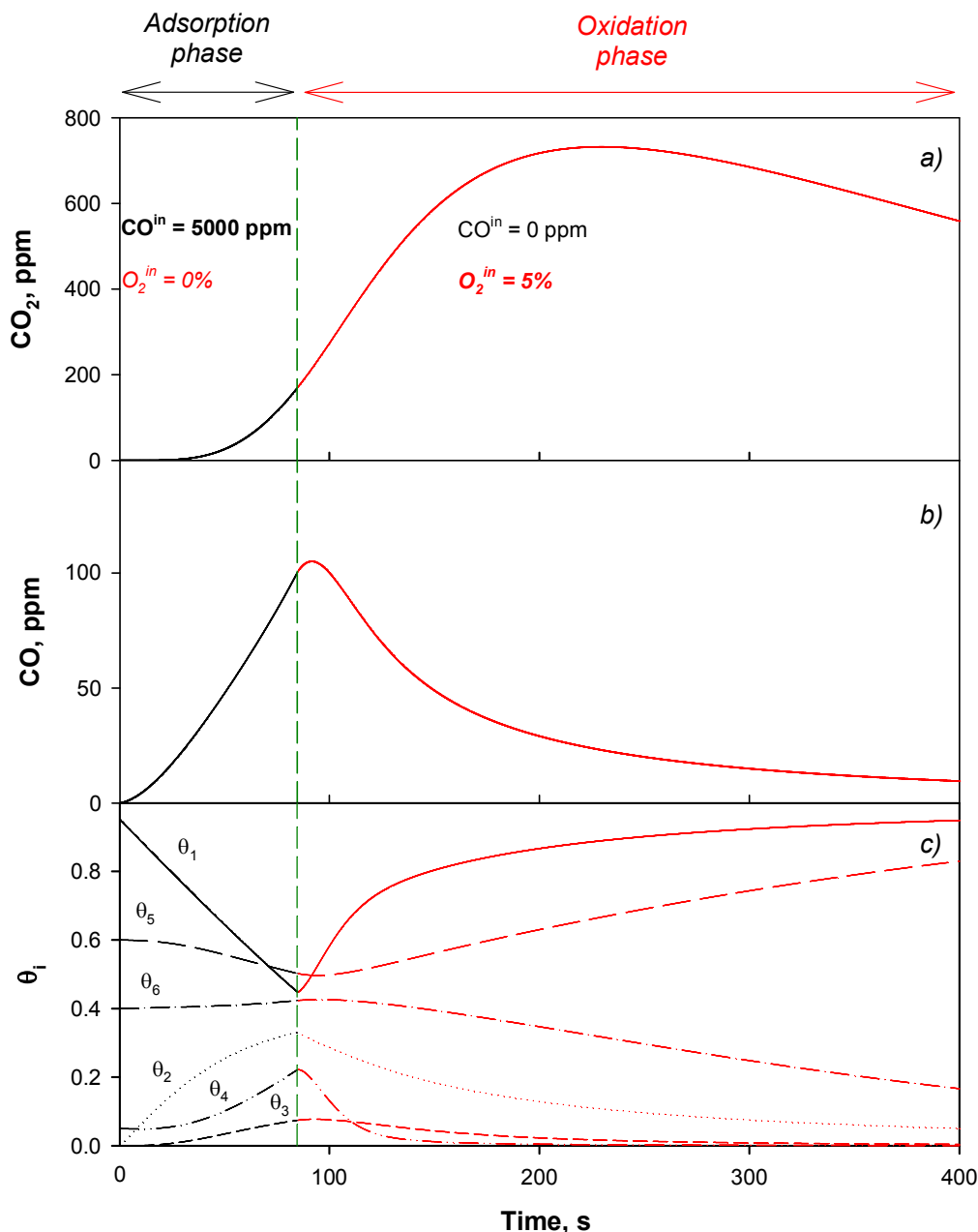


**Figure 13.**  $\text{CO}_2$  (a) and CO (b) outlet concentration and site concentrations (c) as functions of time, complete trap simulation.  $\tau_1 = 95 \text{ s}$ . Adsorption phase:  $\text{CO}^{in} = 5000 \text{ ppm}$  and  $O_2^{in} = 0$ . Oxidation phase:  $\text{CO}^{in} = 0$ ;  $O_2^{in} = 5 \text{ vol.}\%$ .

When the CO outlet concentration reaches 100 ppm, the feed is switched to  $\text{CO}^{in} = 0$  and  $O_2$  is fed (5 vol %).

The corresponding evolution of the catalyst sites is shown in Figure 14 (c and d) as well. During the adsorption phase, we observe that the active sites (sites  $\text{Cu}^{2+}-\text{O}^{2-}-\text{Ce}^{4+}$ ) start to be covered by CO ( $\theta_1$  decreases,  $\theta_2$  increases). The activation of oxygen transfer from the Ce sites to the Cu sites (step 4 of the reaction mechanism) should also be noted, since  $\theta_6$  slightly increases and  $\theta_5$  decreases. CO is present as adsorbed over the catalyst ( $\theta_2$ ) and only partially oxidized to  $\text{CO}_2$  ( $\theta_3$ ).

During the oxidation phase, both the Cu- ( $\theta_1$ ) and Ce- ( $\theta_5$ ) oxidized sites are restored. However, it is worth noting that the time required for reaching the initial values is quite high (~400 s).

In order to optimize the trap operation, we performed simulations of several subsequent cycles. In Figure 15, the adsorption/oxidation cycles are shown as obtained by setting the duration of the oxidation step at 100 s, whereas time length of the adsorption phase is adjusted by the time at which CO outlet concentration reaches 100 ppm, corresponding to about 85 s for the first adsorption phase, in agreement with above results.

From the plot it appears that the amount of CO trapped/converted increases cycle by cycle, as suggested by the increasing length of the adsorption phase (84.6 s; 107.15 s; 462.15 s).

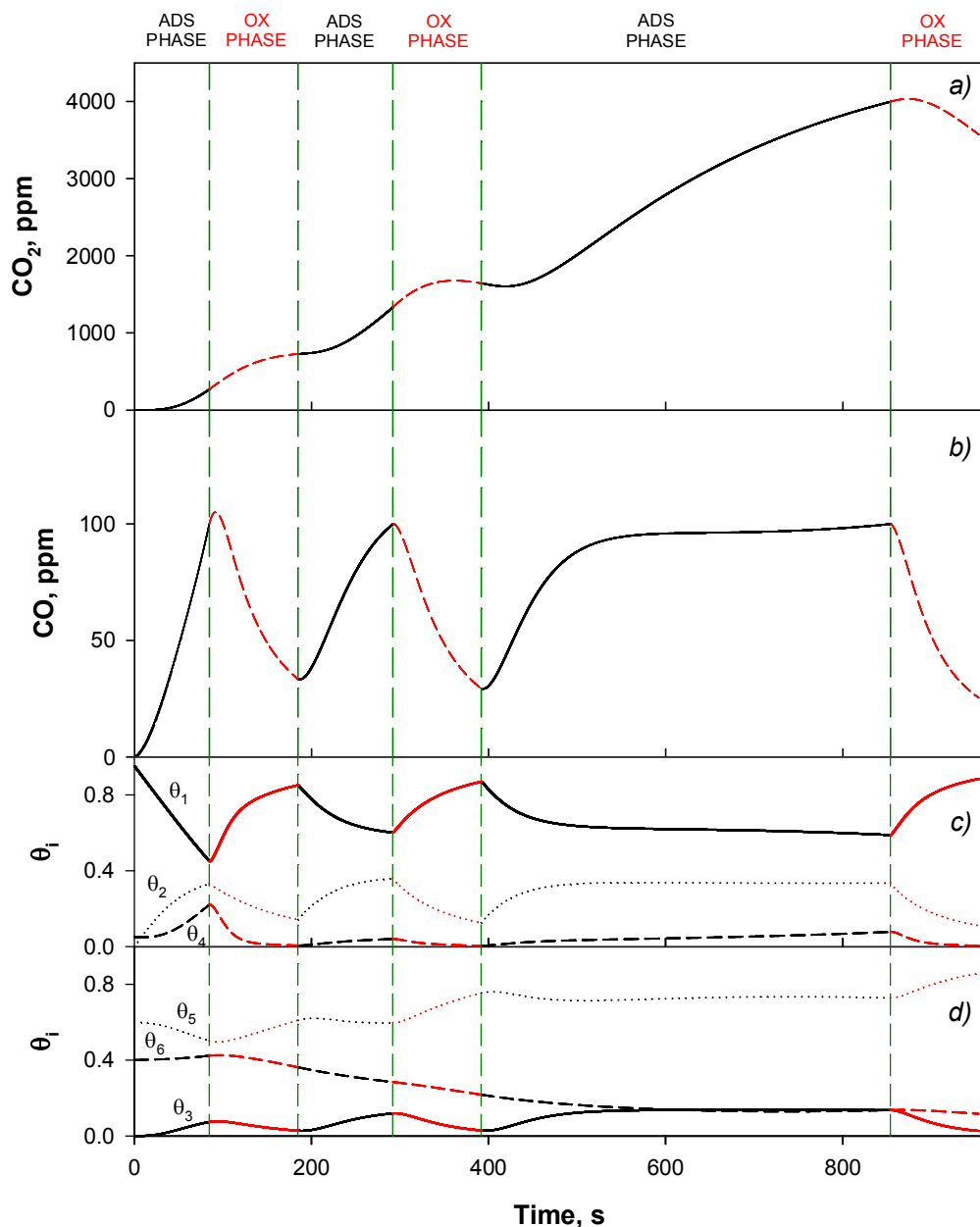


**Figure 14.**  $\text{CO}_2$  (a) and  $\text{CO}$  (b) concentrations and site concentrations (Cu-containing (c) and ceria (d) sites) as functions of time, complete trap simulation.  $\tau_1 = 95$  s. Adsorption phase:  $\text{CO}^{in} = 5000$  ppm and  $\text{O}_2^{in} = 0$ . Oxidation phase:  $\text{CO}^{in} = 0$ ;  $\text{O}_2^{in} = 5$  vol %. Time duration of the oxidation phase = 100 s.

The site concentrations as functions of time during the cycles are shown in Figure 14d as well. Excluding the first adsorption phase,  $\theta_6$  (i.e., reduced ceria sites) steadily decreases cycle by cycle, while oxidized ceria sites ( $\theta_5$ ) and surface carbonates ( $\theta_3$ ) increase on average, thus suggesting that  $\text{CO}_2$

buffering on the surface improves the oxygen storage capacity of the catalyst. Accordingly, the fraction of reduced copper sites ( $\theta_4$ ) is low.

In order to improve the catalyst regeneration, we changed the time length of the oxidation phase. In Figure 15, the trap simulation results are shown in terms of CO and CO<sub>2</sub> concentrations and site distribution as calculated by assuming a double oxidation phase duration (200 s), stopping the adsorption phase when CO concentration reaches 100 ppm as before. Under these conditions, CO adsorption can last more than the oxidation phase starting from the second cycle. This is due to a deeper re-oxidation of the copper sites (Figure 15d) and to the decrease of  $\theta_4$  going down to zero at the end of each oxidation phase. As a consequence, the CO adsorbed/reacted and the CO<sub>2</sub> formed can be the same at each cycle.

The above results suggest that by a proper choice of the regeneration (oxidation) time, the CO trap system could work with only two reactors operated under adsorption/oxidation conditions, as shown in Figure 1.

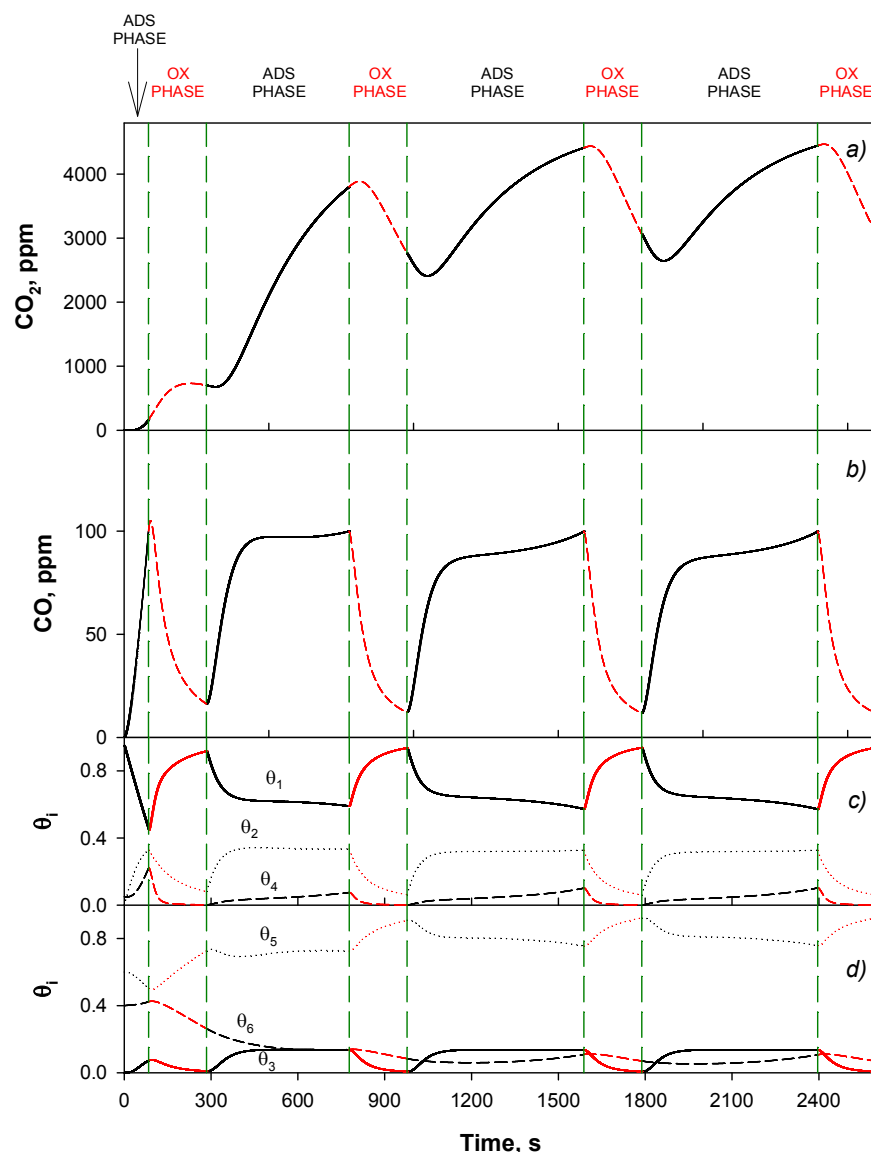


**Figure 15.** CO<sub>2</sub> (a) and CO (b) concentrations and site concentrations (Cu-containing (c) and ceria (d) sites) as functions of time, complete trap simulation.  $\tau_1 = 95$  s. Adsorption phase:  $CO^{in} = 5000$  ppm and  $O_2^{in} = 0$ . Oxidation phase:  $CO^{in} = 0$ ;  $O_2^{in} = 5$  vol %. Time duration of the oxidation phase = 200 s.

From the above results, it appears that the time required to reach 100 ppm is quite high (about 400 s) and that after about 200 s, CO fast reaches 85 ppm, then increasing very slowly up to 100 ppm. We then simulated the trap by fixing the time duration of both the adsorption and the oxidation phase at  $t = 200$  s.

In Figure 16, the CO and  $\text{CO}_2$  concentrations are shown as functions of time as obtained by assuming the first cycle is stopped when CO reaches 100 ppm (about 85 s) and then by switching the feed composition every 200 s.

After a transient phase lasting about 1000 s (corresponding to three adsorption/oxidation cycles), a periodic stable (forced) regime is attained. CO concentration is oscillating between 10 and 85 ppm.

The site concentrations are plotted in Figure 16 as well. It is worth noting that the catalyst is stabilized in the oxidized form,  $\theta_4$  and  $\theta_6$  (reduced sites containing both copper and cerium and only cerium, respectively) being nearly zero. The high oxidation degree of ceria sites ( $\theta_5$ ), oscillating between 0.8 and 0.95, thus behave as an oxygen reservoir for copper sites during the adsorption phase, promoting both CO adsorption and oxidation to  $\text{CO}_2$ .

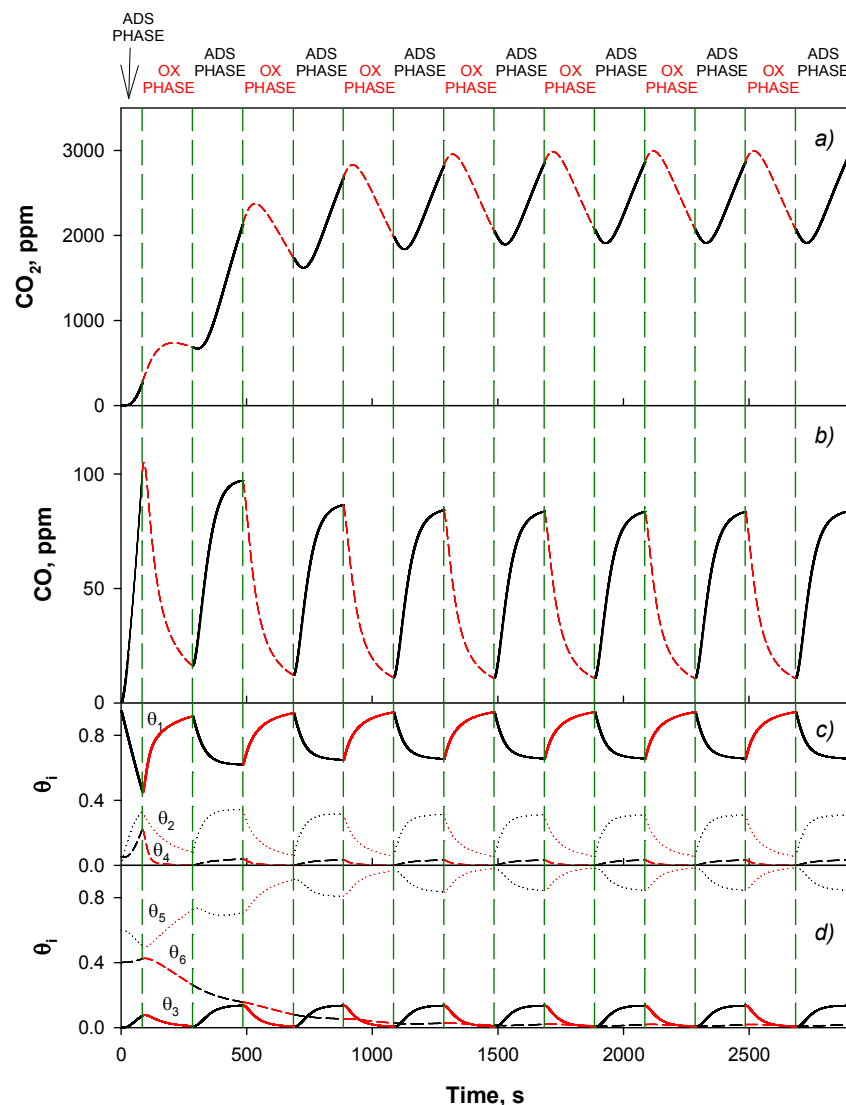


**Figure 16.**  $\text{CO}_2$  (a) and CO (b) concentrations and site concentrations (Cu-containing (c) and ceria (d) sites) as functions of time, complete trap simulation.  $\tau_1 = 95$  s. Adsorption phase:  $\text{CO}^{in} = 5000$  ppm and  $\text{O}_2^{in} = 0$ . Oxidation phase:  $\text{CO}^{in} = 0$ ;  $\text{O}_2^{in} = 5$  vol %. Time duration of both the adsorption and oxidation phases = 200 s (first adsorption excluded).

It should also be noted that, during the oxidation phase, a complete desorption of CO<sub>2</sub> occurs ( $\theta_3 \approx 0$  in the oxidation phase). Conversely, CO is not completely oxidized, since  $\theta_2$  is always higher than zero, even in the oxidation phase. From these results, we may conclude that the key step of the reaction mechanism at these operating conditions is the oxygen transfer from the Ce sites to the Cu sites (step 4).

It is worth noting that according to this trap operation, the valves switching time is 200 s for both phases, which is compatible with the process operation.

When switching from one feed to the other, unavoidable mixing can occur. In particular, when switching from the CO adsorption to the CO oxidation phase, hydrogen still present in the reactor may be mixed with the oxygen-containing stream generating a H<sub>2</sub>/O<sub>2</sub>/N<sub>2</sub> mixture. This mixture represents a loss of H<sub>2</sub> and it could in principle be flammable.

Likewise, when switching from the CO oxidation phase to the CO adsorption phase, a mixture of H<sub>2</sub>/O<sub>2</sub>/N<sub>2</sub>/CO is generated which cannot be fed to the fuel cell and represents a loss of H<sub>2</sub>.

In order to avoid incorrect feeding and H<sub>2</sub> loss, it is crucial to optimize the delay time between the switch of the inlet/outlet valves of the two reactors of the process.

It should be said that immediately after switching, a H<sub>2</sub>/O<sub>2</sub>/N<sub>2</sub>/CO could be formed. In the chosen operating conditions (oxidizing stream containing 5% O<sub>2</sub>), this mixture is not flammable, the oxygen content being lower than the H<sub>2</sub> minimum oxide concentration (MOC = 5%). In any case, this mixture may be generated from air by mixing the outlet steam (containing about 3.5% O<sub>2</sub>) with fresh air.

## 5. Conclusions

In this work, we proposed a novel approach for CO abatement in H<sub>2</sub>-rich streams to be fed to PEM fuel cells. The main concept is a dual-stage process operating with a copper/ceria based catalyst, consisting of a reactive adsorption phase, allowing for CO abatement under the PEM limits, and an oxidation phase, restoring the catalyst and converting the adsorbed CO into CO<sub>2</sub>. By this approach it should be possible to simultaneously get CO lower than the limiting value and avoid any H<sub>2</sub> consumption with no O<sub>2</sub> in the feed stream to the PEM. Parameters of a kinetic model including CO adsorption and oxidation to CO<sub>2</sub>, CO<sub>2</sub> desorption, and catalyst re-oxidation by molecular oxygen, developed on the basis of previous results, were obtained from data of suitably programmed experimental tests. Experimental and model simulations are in good agreement, especially for the CO-reactive adsorption phase.

The simulations were performed at varying operating parameters. The results showed that high contact times and low CO inlet concentration are beneficial in order to obtain CO concentration lower than 100 ppm for long period, as expected. However, due to the non-linear behavior of the CO reactive adsorption, the effect is quantitatively different from that expected for a classical adsorption, in particular, the effect of contact time is more than linear, while that of CO inlet concentration is less than linear.

The simulations of the complete system, varying the time length of the oxidation phase (adsorption phase ending when CO at the outlet reaches 100 ppm followed by the oxidation phase), highlighted the importance of carrying out a deep oxidation in order to fully regenerate the material, restoring the initial oxidation state. Even if CO<sub>2</sub> buffering on the catalyst causes an increase of the mean oxidation state, related to larger and larger adsorption phase duration, by a proper choice of the duration of the oxidation phase, conditions to operate always under the target exit CO concentration (100 ppm) can be found. Consequently, a suitable equal time length can be chosen for the two phases in order to synchronize them and assure a cyclic operation which could be carried out by using only two reactors (one acting as adsorber, the other in regeneration). In this work, we chose 200 s as working time and demonstrated that a stable periodic operation was achieved.

**Author Contributions:** G.L., A.D.B. and L.L. conceived and designed the experiments and the simulations; G.L. and L.L. performed the experiments; A.D.B. developed the model and performed the simulations; G.L., A.D.B. and L.L. analyzed the data; G.L., A.D.B. and L.L. wrote the paper.

**Acknowledgments:** The present work was financially supported by MIUR (Italy) under FIRB projects (project code: RBFR10S4OW—Novel catalytic systems for H<sub>2</sub>-rich streams purification).

**Conflicts of Interest:** The authors declare no conflict of interest.

## References

1. Recupero, V.; Pino, L.; Vita, A.; Cipitì, F.; Cordaro, M.; Laganà, M. Development of a LPG fuel processor for PEFC systems: Laboratory scale evaluation of autothermal reforming and preferential oxidation subunits. *Int. J. Hydrogen Energy* **2005**, *30*, 963–971. [[CrossRef](#)]
2. Pan, L.; Wang, S. A compact integrated fuel-processing system for proton exchange membrane fuel cells. *Int. J. Hydrog. Energy* **2006**, *31*, 447–454. [[CrossRef](#)]
3. Men, Y.; Kolb, G.; Zapf, R.; Tiemann, D.; Wichert, M.; Hessel, V.; Lowe, H. A complete miniaturized microstructured methanol fuel processor/fuel cell system for low power applications. *Int. J. Hydrogen Energy* **2008**, *33*, 1374–1382. [[CrossRef](#)]
4. Oliva, D.G.; Francesconi, J.A.; Mussati, M.C.; Aguirre, P.A. Energy efficiency analysis of an integrated glycerin processor for PEM fuel cells: Comparison with an ethanol-based system. *Int. J. Hydrogen Energy* **2010**, *35*, 709–724. [[CrossRef](#)]
5. Di Bona, D.; Jannelli, E.; Minutillo, M.; Perna, A. Investigations on the behaviour of 2kW natural gas fuel processor. *Int. J. Hydrogen Energy* **2011**, *36*, 7763–7770. [[CrossRef](#)]
6. Ji, H.; Bae, J.; Cho, S.; Kang, I. Start-up strategy and operational tests of gasoline fuel processor for auxiliary power unit. *Int. J. Hydrogen Energy* **2015**, *40*, 4101–4110. [[CrossRef](#)]
7. Yan, C.; Hai, H.; Guo, C.; Li, W.; Huang, S.; Chen, H. Hydrogen production by steam reforming of dimethyl ether and CO-PrOx in a metal foam micro-reactor. *Int. J. Hydrogen Energy* **2014**, *39*, 10409–10416. [[CrossRef](#)]
8. Engelhardt, P.; Maximini, M.; Beckmann, F.; Brenner, M.; Moritz, O. Coupled operation of a diesel steam reformer and an LT- and HT-PEFC. *Int. J. Hydrogen Energy* **2014**, *39*, 18146–18153. [[CrossRef](#)]
9. Trimm, D.L.; Önsan, Z.I. Onboard Fuel Conversion for Hydrogen-Fuel-Cell-Driven Vehicles. *Catal. Rev. Sci. Eng.* **2001**, *43*, 31–84. [[CrossRef](#)]
10. Zhao, Z.; Lin, X.; Jin, R.; Dai, Y.; Wang, G. High catalytic activity in CO PROX reaction of low cobalt-oxide loading catalysts supported on nano-particulate CeO<sub>2</sub>–ZrO<sub>2</sub> oxides. *Catal. Commun.* **2011**, *12*, 1448–1451. [[CrossRef](#)]
11. López, I.; Valdés-Solís, T.; Marbán, G. An attempt to rank copper-based catalysts used in the CO-PROX reaction. *Int. J. Hydrogen Energy* **2008**, *33*, 197–205. [[CrossRef](#)]
12. Lukashuk, L.; Föttinger, K.; Kolar, E.; Rameshan, C.; Teschner, D.; Hävecker, M.; Knop-Gericke, A.; Yigit, N.; Li, H.; McDermotta, E. Operando XAS and NAP-XPS studies of preferential CO oxidation on Co<sub>3</sub>O<sub>4</sub> and CeO<sub>2</sub>–Co<sub>3</sub>O<sub>4</sub> catalysts. *J. Catal.* **2016**, *344*, 1–15. [[CrossRef](#)]
13. Martínez-Arias, A.; Fernández-García, M.; Galvez, O.; Coronado, J.M.; Anderson, J.A.; Conesa, J.C.; Munuera, S.G. Comparative study on redox properties and catalytic behavior for CO oxidation of CuO/CeO<sub>2</sub> and CuO/ZrCeO<sub>4</sub> catalysts. *J. Catal.* **2000**, *195*, 207–216. [[CrossRef](#)]
14. Sedmak, G.; Hočevá, S.; Levec, J. Kinetics of selective CO oxidation in excess of H<sub>2</sub> over the nanostructured Cu<sub>0.1</sub>Ce<sub>0.9</sub>O<sub>2-y</sub> catalyst. *J. Catal.* **2003**, *213*, 135–150. [[CrossRef](#)]
15. Caputo, T.; Lisi, L.; Pirone, R.; Russo, G.; Ii, F. Kinetics of the Preferential Oxidation of CO over CuO/CeO<sub>2</sub> Catalysts in H<sub>2</sub>-Rich. *Ind. Eng. Chem. Res.* **2007**, *46*, 6793–6800. [[CrossRef](#)]
16. Martínez-Arias, A.; Hungría, A.B.; Fernández-García, M.; Conesa, J.C.; Munuera, G. Preferential oxidation of CO in a H<sub>2</sub>-rich stream over CuO/CeO<sub>2</sub> and CuO/(Ce,M)Ox (M = Zr, Tb) catalysts. *J. Power Sources* **2005**, *151*, 32–42. [[CrossRef](#)]
17. Martínez-Arias, A.; Hungría, A.B.; Munuera, G.; Gamarra, D. Preferential oxidation of CO in rich H<sub>2</sub> over CuO/CeO<sub>2</sub>: Details of selectivity and deactivation under the reactant stream. *Appl. Catal. B Environ.* **2006**, *65*, 207–216. [[CrossRef](#)]

18. Moretti, E.; Lenarda, M.; Riello, P.; Storaro, L.; Talon, A.; Frattini, R.; Reyes-Carmon, A.; Jiménez-López, A.; Rodríguez-Castellón, E. Influence of synthesis parameters on the performance of CeO<sub>2</sub>-CuO and CeO<sub>2</sub>-ZrO<sub>2</sub>-CuO systems in the catalytic oxidation of CO in excess of hydrogen. *Appl. Catal. B Environ.* **2013**, *129*, 556–565. [[CrossRef](#)]
19. Avgouropoulos, G.; Ioannides, T.; Matralis, H. Influence of the preparation method on the performance of CuO-CeO<sub>2</sub> catalysts for the selective oxidation of CO. *Appl. Catal. B Environ.* **2005**, *56*, 87–93. [[CrossRef](#)]
20. Liu, Z.; Zhou, R.; Zheng, X. Influence of rare-earth metal doping on the catalytic performance of CuO-CeO<sub>2</sub> for the preferential oxidation of CO in excess hydrogen. *J. Nat. Gas. Chem.* **2008**, *17*, 283–287. [[CrossRef](#)]
21. Reddy, L.H.; Reddy, G.K.; Devaiah, D.; Reddy, B.M. A rapid microwave-assisted solution combustion synthesis of CuO promoted CeO<sub>2</sub>-MxOy (M = Zr, La, Pr and Sm) catalysts for CO oxidation. *Appl. Catal. A Gen.* **2012**, *445*:446, 297–305. [[CrossRef](#)]
22. Avgouropoulos, G.; Ioannides, T.; Matralis, H.K.; Batista, J.; Hocevar, S. CuO-CeO<sub>2</sub> mixed oxide catalysts for the selective oxidation of carbon monoxide in excess hydrogen. *Catal. Lett.* **2001**, *73*, 33–40. [[CrossRef](#)]
23. Zou, H.; Dong, X.; Lin, W. Selective CO oxidation in hydrogen-rich gas over CuO/CeO<sub>2</sub> catalysts. *Appl. Surf. Sci.* **2006**, *253*, 2893–2898. [[CrossRef](#)]
24. Avgouropoulos, G.; Ioannides, T. Selective CO oxidation over CuO-CeO<sub>2</sub> catalysts prepared via the urea–nitrate combustion method. *Appl. Catal. A Gen.* **2003**, *244*, 155–167. [[CrossRef](#)]
25. Gurbani, A.; Ayastuy, J.L.; González-Marcos, M.P.; Gutiérrez-Ortiz, M.A. CuO-CeO<sub>2</sub> catalysts synthesized by various methods: Comparative study of redox properties. *Int. J. Hydrogen Energy* **2010**, *35*, 11582–11590. [[CrossRef](#)]
26. Marban, G.; Fuertes, A.B. Highly active and selective CuOx/CeO<sub>2</sub> catalyst prepared by a single-step citrate method for preferential oxidation of carbon monoxide. *Appl. Catal. B Environ.* **2005**, *57*, 43–53. [[CrossRef](#)]
27. Barbato, P.S.; Colussi, S.; Di Benedetto, A.; Landi, G.; Lisi, L.; Llorca, J.; Trovarelli, A. Origin of High Activity and Selectivity of CuO/CeO<sub>2</sub> Catalysts Prepared by Solution Combustion Synthesis in CO-PROX Reaction. *J. Phys. Chem. C* **2016**, *120*, 13039–13048. [[CrossRef](#)]
28. Landi, G.; Di Benedetto, A.; Colussi, S.; Barbato, P.S.; Lisi, L. Effect of carbon dioxide and water on the performances of an iron-promoted copper/ceria catalyst for CO preferential oxidation in H<sub>2</sub>-rich streams. *Int. J. Hydrogen Energy* **2016**, *41*, 7332–7341. [[CrossRef](#)]
29. Barbato, P.S.; Colussi, S.; Di Benedetto, A.; Landi, G.; Lisi, L.; Llorca, J.; Trovarelli, A. CO preferential oxidation under H<sub>2</sub>-rich streams on copper oxide supported on Fe promoted CeO<sub>2</sub>. *Appl. Catal. A Gen.* **2015**, *506*, 268–277. [[CrossRef](#)]
30. Wang, W.-W.; Du, P.-P.; Zou, S.-H.; He, H.-Y.; Wang, R.-X.; Jin, Z.; Shi, S.; Huang, Y.-Y.; Si, S.; Song, Q.-S. Highly Dispersed Copper Oxide Clusters as Active Species in Copper-Ceria Catalyst for Preferential Oxidation of Carbon Monoxide. *ACS Catal.* **2015**, *5*, 2088–2099. [[CrossRef](#)]
31. Elias, J.S.; Artrith, N.; Bugnet, M.; Giordano, L.; Botton, G.A.; Kolpak, A.M.; Yang, S.H. Elucidating the Nature of the Active Phase in Copper/Ceria Catalysts for CO Oxidation. *ACS Catal.* **2016**, *6*, 1675–1679. [[CrossRef](#)]
32. Davó-Quiñonero, A.; Navlani-García, M.; Lozano-Castelló, D.; Bueno-López, A.; Anderson, J.A. Role of Hydroxyl Groups in the Preferential Oxidation of CO over Copper Oxide-Cerium Oxide Catalysts. *ACS Catal.* **2016**, *6*, 1723–1731. [[CrossRef](#)]
33. Lee, H.C.; Kim, D.H. Kinetics of CO and H<sub>2</sub> oxidation over CuO-CeO<sub>2</sub> catalyst in H<sub>2</sub> mixtures with CO<sub>2</sub> and H<sub>2</sub>O. *Catal. Today* **2008**, *132*, 109–116. [[CrossRef](#)]
34. Di Benedetto, A.; Landi, G.; Lisi, L.; Russo, G. Role of CO<sub>2</sub> on CO preferential oxidation over CuO/CeO<sub>2</sub> catalyst. *Appl. Catal. B Environ.* **2013**, *142*–*143*, 169–177. [[CrossRef](#)]
35. Wang, J.B.; Lin, S.C.; Huang, T.J. Selective CO oxidation in rich hydrogen over CuO/samaria-doped ceria. *Appl. Catal. A Gen.* **2002**, *232*, 107–120. [[CrossRef](#)]
36. Chuang, C.; Chen, Y.; Ward, J.; Yu, C.; Liu, Y.; Lee, C. Optimal design of an experimental methanol fuel reformer. *Int. J. Hydrogen Energy* **2008**, *33*, 7062–7073. [[CrossRef](#)]
37. Dudýeld, C.D.; Chen, R.; Adcock, P.L. A carbon monoxide PROX reactor for PEM fuel cell automotive application. *Int. J. Hydrogen Energy* **2001**, *26*, 763–775. [[CrossRef](#)]
38. Northrop, W.F.; Choi, S.O.; Thompson, L.T. Thermally integrated fuel processor design for fuel cell applications. *Int. J. Hydrogen Energy* **2012**, *37*, 3447–3458. [[CrossRef](#)]

39. Cipiti, F.; Pino, L.; Vita, A.; Laganà, M.; Recupero, V. Experimental investigation on a methane fuel processor for polymer electrolyte fuel cells. *Int. J. Hydrogen Energy* **2013**, *38*, 2387–2397. [[CrossRef](#)]
40. Ayastuy, J.L.; Gurbani, A.; González-Marcos, M.P.; Gutiérrez-Ortiz, M.A. Selective CO oxidation in H<sub>2</sub> streams on CuO/Ce<sub>x</sub>Zr<sub>1-x</sub>O<sub>2</sub> catalysts: Correlation between activity and low temperature reducibility. *Int. J. Hydrogen Energy* **2012**, *37*, 1993–2006. [[CrossRef](#)]
41. Sirichaiprasert, K.; Luengnaruemitchai, A.; Pongstabodee, S. Selective oxidation of CO to CO<sub>2</sub> over Cu-Ce-Fe-O composite-oxide catalyst in hydrogen feed stream. *Int. J. Hydrogen Energy* **2007**, *32*, 915–926. [[CrossRef](#)]
42. Lendzion-Bielun, Z.; Bettahar, M.M.; Monteverdi, S. Fe-promoted CuO/CeO<sub>2</sub> catalyst: Structural characterization and CO oxidation activity. *Catal. Commun.* **2010**, *11*, 1137–1142. [[CrossRef](#)]
43. Zou, H.; Chen, S.; Liu, Z.; Lin, W. Selective CO oxidation over CuO-CeO<sub>2</sub> catalysts doped with transition metal oxides. *Powder Technol.* **2011**, *207*, 238–244. [[CrossRef](#)]
44. Kydd, R.; Ferri, D.; Hug, P.; Scott, J.; Teoh, W.Y.; Amal, R. Temperature-induced evolution of reaction sites and mechanisms during preferential oxidation of CO. *J. Catal.* **2011**, *277*, 64–71. [[CrossRef](#)]
45. Zhang, Q.; Shore, L.; Farrauto, R.J. Selective CO oxidation over a commercial PROX monolith catalyst for hydrogen fuel cell applications. *Int. J. Hydrogen Energy* **2012**, *37*, 10874–10880. [[CrossRef](#)]
46. Caputo, T.; Lisi, L.; Pirone, R.; Russo, G. On the role of redox properties of CuO/CeO<sub>2</sub> catalysts in the preferential oxidation of CO in H<sub>2</sub>-rich gases. *Appl. Catal. A Gen.* **2008**, *348*, 42–53. [[CrossRef](#)]
47. Gamarra, D.; Munuera, G.; Hungría, A.B.; Fernández-García, M.; Conesa, J.C.; Midgley, P.A.; Wang, X.Q.; Hanson, J.C.; Rodríguez, J.A.; Martínez-Arias, A. Structure-activity relationship in nanostructured copper-ceria-based preferential CO oxidation catalysts. *J. Phys. Chem. C* **2007**, *111*, 11026–11038. [[CrossRef](#)]
48. Di Benedetto, A.; Landi, G.; Lisi, L. CO reactive adsorption at low temperature over CuO/CeO<sub>2</sub> structured catalytic monolith. *Int. J. Hydrogen Energy* **2017**. [[CrossRef](#)]
49. Landi, G.; Barbato, P.S.; Di Benedetto, A.; Lisi, L. Optimization of the preparation method of CuO/CeO<sub>2</sub> structured catalytic monolith for CO preferential oxidation in H<sub>2</sub>-rich streams. *Appl. Catal. B Environ.* **2016**, *181*, 727–737. [[CrossRef](#)]
50. Barbato, P.S.; Di Benedetto, A.; Landi, G.; Lisi, L. CuO/CeO<sub>2</sub> based monoliths for CO preferential oxidation in H<sub>2</sub>-rich streams. *Chem. Eng. J.* **2015**, *279*, 983–993. [[CrossRef](#)]
51. Arango-Díaz, A.; Cecilia, J.A.; Dos Santos-Gómez, L.; Marrero-López, D.; Losilla, E.R.; Jiménez-Jiménez, J.; Rodríguez-Castellóna, E. Characterization and performance in preferential oxidation of CO of CuO-CeO<sub>2</sub> catalysts synthesized using polymethyl metacrylate (PMMA) as template. *Int. J. Hydrogen Energy* **2015**, *40*, 11254–11260. [[CrossRef](#)]
52. Moreno, M.; Bergamini, L.; Baronetti, G.T.; Laborde, M.A.; Mariño, F.J. Mechanism of CO oxidation over CuO/CeO<sub>2</sub> catalysts. *Int. J. Hydrogen Energy* **2010**, *35*, 5918–5924. [[CrossRef](#)]
53. Kanervo, J.M.; Keskitalo, T.J.; Slloor, R.I.; Krause, A.O.I. Temperature-programmed desorption as a tool to extract quantitative kinetic or energetic information for porous catalysts. *J. Catal.* **2006**, *238*, 382–393. [[CrossRef](#)]



© 2018 by the authors. Licensee MDPI, Basel, Switzerland. This article is an open access article distributed under the terms and conditions of the Creative Commons Attribution (CC BY) license (<http://creativecommons.org/licenses/by/4.0/>).